

Effects of Vehicle Weight and True Versus Indicated Airspeed on BVI Noise During Steady Descending Flight

James H. Stephenson

US Army

Aviation Development Directorate
Aviation & Missile Research,
Development & Engineering Center
Hampton, VA

Eric Greenwood

Aeroacoustics Branch

NASA Langley Research Center
Hampton, VA

Blade-vortex interaction noise measurements are analyzed for an AS350B helicopter operated at 7000 ft elevation above sea level. Blade-vortex interaction (BVI) noise from four, 6 degree descent conditions are investigated with descents flown at 80 knot true and indicated airspeed, as well as 4400 and 3915 pound take-off weights. BVI noise is extracted from the acquired acoustic signals by way of a previously developed time-frequency analysis technique. The BVI extraction technique is shown to provide a better localization of BVI noise, compared to the standard Fourier transform integration method. Using this technique, it was discovered that large changes in BVI noise amplitude occurred due to changes in vehicle gross weight. Changes in BVI noise amplitude were too large to be due solely to changes in the vortex strength caused by varying vehicle weight. Instead, it is suggested that vehicle weight modifies the tip-path-plane angle of attack, as well as induced inflow, resulting in large variations of BVI noise. It was also shown that defining flight conditions by true airspeed, rather than indicated airspeed, provides more consistent BVI noise signals.

Background

The rotorcraft community is continually focused on the understanding, prediction, and mitigation of various noise mechanisms, including blade-vortex interaction (BVI) noise (Refs. 1–4). BVI occurs when a previously generated tip vortex impinges on a subsequent rotor blade (Ref. 5). This results in an impulsive aerodynamic load on the rotor blade, generating vehicle vibratory loads and noise (Refs. 6, 7). BVI noise results in high community annoyance levels in and around civilian heliports, which poses limitations on the allowable flight operations.

Ideally, BVI noise should be investigated in isolation from other noise sources, to better understand mechanisms that affect emitted BVI noise. Separation of noise sources can be difficult when full-scale flight tests are performed as the measured acoustic signals simultaneously include all vehicle, and ambient, noise sources. Several methods have been developed in order to extract the BVI noise signal from acquired acoustic signals (Refs. 8–10). Here, the BVI extraction method developed in Ref. 10, which was inspired by Ref. 8, will be used.

This BVI extraction technique employs a time-scale analysis method to localize BVI pulses in the time-frequency domain. The time-scale analysis technique employed is

AHS 71st Annual Forum, Virginia Beach, USA, May 5-7, 2015. This is a work of the U.S. Government and is not subject to copyright protection in the U.S. DISTRIBUTION STATEMENT TBD.

the wavelet transform, which convolves an *a priori* known ‘mother’ wavelet (ψ_w), with the pressure time series ($p(t)$). This convolution is given as

$$\tilde{p}(l, t) = \frac{1}{\sqrt{l}} \int_{-\infty}^{\infty} p(t') \psi_w^*\left(\frac{t'-t}{l}\right) dt', \quad (1)$$

where l is the scale of the wavelet and $\tilde{p}(l, t)$ are the wavelet coefficients.

There are an infinite number of wavelets available to use, but only the Morlet wavelet with a non-dimensional frequency (ω_ψ) of 6 will be used here. The Morlet wavelet is chosen as it has previously been shown to adequately characterize helicopter acoustic signals in the time-frequency domain (Ref. 11). Further, the Morlet wavelet has a known one to one scale to frequency transformation, such that $\tilde{p}(l, t) \rightarrow \tilde{p}(f, t)$. The frequency domain representation of the Morlet wavelet ($\hat{\psi}_M$) is defined by Ref. 12 as

$$\hat{\psi}_M(l, \omega, \omega_\psi) = \sqrt{2\pi l \frac{f_s}{N}} \pi^{-1/4} H(\omega) e^{-(l\omega - \omega_\psi)^2/2}, \quad (2)$$

where N is the number of samples in the data set, f_s is the sampling rate, and $H(\omega)$ is the Heaviside function. The scale-normalized energy density ($E(f, t)$) is given as

$$E(f, t) = \frac{1}{C_\psi} \frac{|\tilde{p}(f, t)|^2}{l^2}, \quad (3)$$

and is analogous to the power spectral density function, with units of pressure squared per hertz. Here, C_ψ is the admissibility factor, and is unique for each mother wavelet (Refs. 12, 13).

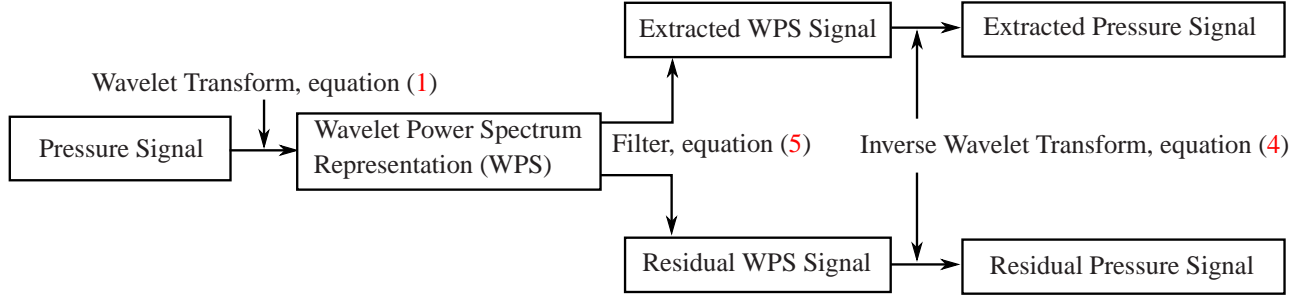


Fig. 1: Schematic diagram of the full BVI extraction process, from original pressure signal through to the extracted signals.

The inverse wavelet transform is given as

$$p(t') = \frac{1}{C_\psi} \int_{-\infty}^{\infty} \int_l \frac{1}{\sqrt{l'}} \tilde{p}(l', t) \psi_w\left(\frac{t' - t}{l'}\right) \frac{dl' dt}{l'^2}, \quad (4)$$

and can be used to recreate a portion, or all, of the original pressure signal. Thus, signals identified in the time–frequency domain can be extracted and their associated pressure time series recreated. The BVI extraction technique, described in Ref. 11 and more completely in Ref. 14, operates on this principle. The BVI signal is identified in the time–frequency domain, extracted, and its pressure time series is recreated. Thus, an acoustic pressure signal containing only BVI is generated.

The BVI extraction technique identifies and extracts the high-frequency, high-amplitude content of the BVI signal. It was shown in Ref. 14 that this adequately removes the BVI signal from the unfiltered pressure time history. The filter is described as

$$\tilde{p}(f_j, t_i) = \begin{cases} \tilde{p}(f_j, t_i) & \text{if } f_j > f_{cut} \text{ and} \\ & E(f_j, t_i) > E(f_{MR}, t_i) - A_{cut}, \\ 0 & \text{otherwise} \end{cases}, \quad (5)$$

where the extracted signal must simultaneously satisfy a frequency (f_{cut}) and amplitude (A_{cut}) cutoff. The frequency cutoff is typically based on harmonics of the main rotor frequency (f_{MR}), while the amplitude cutoff A_{cut} is relative to the energy in the main rotor fundamental harmonic signal, at each instant in time ($E(f_{MR}, t_i)$). It was seen previously in Ref. 10 that the wavelet-transformed energy in the BVI signal, when present, is on the same order of magnitude as the energy in the main rotor blade pass frequency. Thus, the amplitude cutoff is allowed to vary in time to match the varying strength of the signal at the main rotor blade pass frequency.

A complete schematic of the extraction technique is provided in figure 1 showing the original pressure signature transformed through the use of the wavelet transform via equation (1), filtered via equation (5), and then inverse transformed via equation (4) to create the associated pressure series.

Technical Approach

NASA Langley and the U.S. Army Aviation Development Directorate conducted a complimentary set of full-scale flight

tests on a Eurocopter AS350B (AStar) and EH-60L vehicles at three test sites over a period stretching from September 2014 through February 2015. The primary objective of the overall experiment is to determine effects of density-altitude variation on helicopter acoustic emissions. The three test sites chosen for this set of experiments are Sweetwater, NV (7000 ft elevation), Sierra Army Depot, CA (4000 ft elevation) and Salton Sea, CA (sea level). Only data from the Sweetwater, NV location will be used here.

Primary focus for this paper, will be on data acquired from the AStar vehicle at Sweetwater, NV. The AStar has a 3-bladed main rotor with an empty weight of 2690 pounds. Further rotor specifications for the AS350B are provided in Table 1. At each site, both vehicles were flown at two dif-

Table 1: AS350B main (MR) and tail (TR) rotor specifications.

	MR	TR	
Number of Blades	3	2	
Radius (R)	10.69	1.86	[m]
Blade Pass Frequency (f)	19.5	104	[Hz]

ferent take-off weights. The nominal value was flown at each test location, while the second weight was calibrated to match weight coefficients (C_w) between the three locations. The AStar’s nominal take-off weight was 4400 lb, with the calibrated weight for the Sweetwater, NV location being 3915 lb ($C_w = 3.68 \cdot 10^{-3}$).

Acoustic data was acquired by 25 Wireless Acoustic Measurement Systems (WAMS). Each WAMS module contains a 15 inch diameter ground board, with a 1/2 inch B&K type 4189 free-field microphone. Each microphone was inverted 1/4 inch above the ground board, and has a dynamic range from 16.5 dB to 134 dB with a frequency range from 20 Hz to 20 kHz. Each WAMS unit contains a GPS receiver for accurate timing between sensors. Microphones were sampled at 25 kHz with 16 bit resolution.

A newly implemented air-data boom was installed on the AStar vehicle and acquired outside air temperature, static and dynamic pressures, along with local wind velocities at a 5 Hz sampling rate. NASA’s Aircraft Navigation and Tracking System (ANTS) was also installed inside the vehicle. ANTS

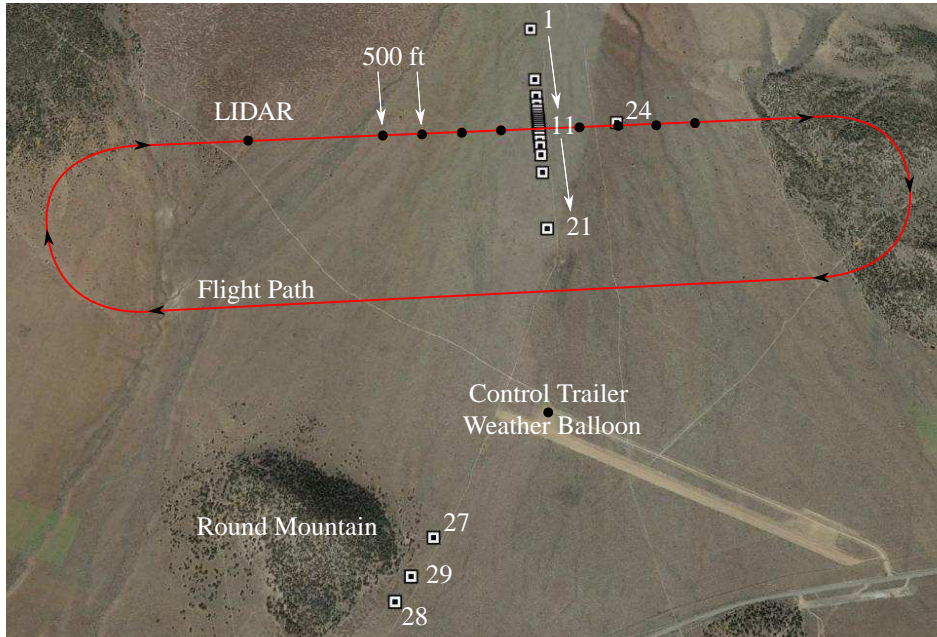


Fig. 2: Equipment locations with notional vehicle flight path and local geography shown.

records vehicle GPS along with inertial navigation data, including vehicle roll and pitch attitudes as well as rates of change. The ANTS module was sampled continuously and uninterrupted throughout the flight day at a rate of 20 Hz. All data is synced to UTC time, and the microphone data is de-Dopplerized and corrected for spherical spreading loss using a previously developed time-domain de-Dopplerization technique (Ref. 15). This method simultaneously transforms the data from time of reception to time of emission, allowing vehicle state data to be directly related to its acoustic impacts. This method is used to transform data acquired while the vehicle is within 2000 ft of the microphone array to a uniform distance of 100 ft.

Local weather data was acquired through the use of a weather balloon with weather sonde, and a ZephIR 300 LIDAR system. The weather balloon was held stationary at 200 ft above ground level, with temperature sensors spaced every 50 ft up the tether to acquire a temperature profile. The weather sonde on the weather balloon acquired local wind velocities, air temperature, pressure, and humidity. The LIDAR system was located underneath the vehicle flight path, 4000 ft in front of the main microphone array. The LIDAR system measures wind velocity at 12 altitudes ranging from zero to 985 ft. Average wind velocities are calculated every ten minutes and linearly interpolated to generate a wind profile at the time of each run. Wind speeds never exceeded 9 knots for the Sweetwater, NV location.

The microphone locations along with LIDAR, weather balloon, and control trailer locations are shown in figure 2. A notional vehicle ground track with markers showing every 500 ft of flight path approaching the main microphone array is also provided. The main microphone array comprises 21 microphones stretching 3000 ft across the flight path. Three micro-

phones, numbers 27-29, were placed behind Round Mountain to capture the effects of diffraction around an isolated hill.

Only data from the 21 microphones on the main array are presented. Further, while 11 distinct flight profiles were flown at Sweetwater, NV, only the four descent conditions are investigated here. Each descent condition was flown at 6 degree flight path angle, with descents nominally occurring at both 80 knots indicated airspeed (KIAS) and 80 knots true airspeed (KTAS). Each run profile was flown for both the nominal and calibrated weight configurations. The AStar burned approximately 280 pounds of fuel at each take-off weight configuration before refueling.

BVI Extraction Results

The BVI extraction technique described in equation (5) is applied to each descent condition using $f_{cut} = 11 f_{MR}$ and $A_{cut} = -6$ dB. The cutoff criteria are chosen for the AS350 as they extract BVI signals with minimal peak to peak pressure amplitude degradation and tail rotor presence in the extracted noise signal.

A Lambert projection of the sound pressure level of the extracted BVI signal from a single, 80 KIAS, 4400 pound take-off weight run, is provided in figure 3a. Sound pressure levels of the extracted BVI signal are calculated by integrating the scale-normalized energy density, which is analogous to integrating the power spectral density function.

The AStar main rotor rotates clockwise when viewed from above, so the Lambert projection starts with an azimuth of 0° at the tail, 90° is to the left (advancing) side of the vehicle, 180° is directly ahead with 270° to the right (retreating) side of the vehicle. Elevation begins in the plane of the rotor (0°) at the edge of the Lambert projection and decreases radially

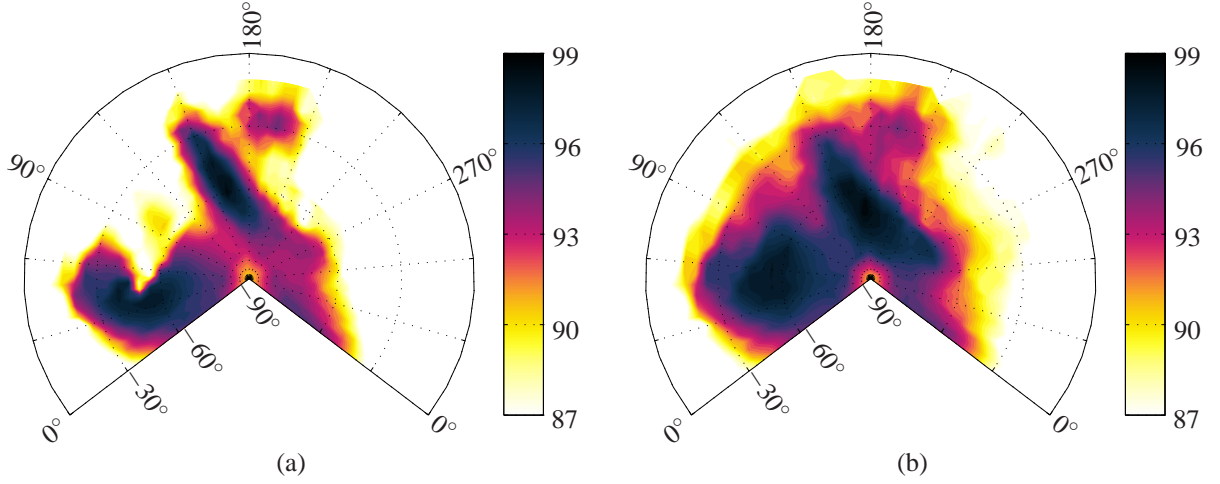


Fig. 3: Lambert projection of sound pressure level [dB] calculated from (a) extracted and (b) standard BVISPL FFT metric.

such that directly beneath the rotor (-90°) is represented by the point in the center of the Lambert projection.

A comparable calculation for the same run was made using the standard blade-vortex interaction sound pressure level (BVISPL) metric. The BVISPL metric, shown in figure 3b, is the power spectral density of the raw pressure signal integrated above f_{cut} , to stay consistent with the BVI extraction technique. Figure 3b identifies the two major BVI hotspots seen in figure 3a, except it is further corrupted by the presence of non-main rotor harmonic noise in azimuthal angles from 90° to 120° . Both methods identify BVI on the rear, advancing side of the rotor disk at approximately 30° azimuth and -60° elevation. However, the forward propagating BVI signals peak lower (-60° elevation) beneath the rotor in the standard method than seen in the BVI extraction method (-45° elevation).

Raw and BVI extracted pressure signals are identified from around the hemisphere in order to investigate the discrepancies seen between these figures. Figure 4 shows the BVI extracted Lambert projection with various pressure signals identified from around the hemisphere. Each subplot provides the original pressure signal (top), as well as the BVI extracted signal (bottom). Each pressure signal encompasses slightly more than a rotor revolution, and is normalized in time such that each signal arbitrarily starts at 0 seconds.

Discussion of figure 4 will progress with increasing azimuth (clockwise), around the Lambert projection, in the same direction of the rotor rotation. The BVI extraction technique identified and cleanly removed BVI occurring at an azimuth and elevation of ($5^\circ, -70^\circ$). BVI here has a peak to peak pressure of approximately 14 Pa, and is identified by similar relative amplitudes in both the extracted and standard BVISPL metrics shown in figure 3. At ($10^\circ, -30^\circ$), very minor BVI exists and again both metrics agree, showing very little BVI energy in their respective Lambert projections. Analysis from the next three locations ($(30^\circ, -45^\circ)$, $(50^\circ, -35^\circ)$, $(60^\circ, -50^\circ)$) can be grouped together as both metrics identify strong BVI noise, with the extracted BVI pressure signal suggesting that one BVI event results in the noise propagating in

this direction. This is suggested as the signal shape remains similar and exists continuously throughout this intense BVI noise region. However, this is not the case entirely as a secondary BVI noise signal becomes evident at ($60^\circ, -50^\circ$), near the end of each primary BVI pulse. An artificial “notch” in the signal envelope can be seen near ($65^\circ, -55^\circ$), but is most likely an interpolation issue, as no microphone was located in the direction of the blank space.

The next notable section occurs at locations ($(100^\circ, -30^\circ)$ and $(105^\circ, -55^\circ)$) where the extracted technique shows very minor BVI occurring, but the standard BVISPL FFT metric, shown in figure 3b, portrays a very strong BVI signal. The raw and extracted pressure signals demonstrate that there is little BVI noise in this region, but there are strong higher frequency components in the raw signal. Thus, the BVISPL FFT metric is keying on these non-rotor harmonic components, and identifying a false BVI noise signal.

Forward propagating BVI noise can be seen in locations ($(150^\circ, -35^\circ)$ and $(180^\circ, -70^\circ)$). BVI noise is removed cleanly by the extraction technique at $(150^\circ, -35^\circ)$, but is corrupted some by higher frequencies in location $(180^\circ, -70^\circ)$. This strong higher frequency energy further corrupts the BVISPL FFT metric, as its energy is incorporated into the SPL integration. This causes the shift in peak BVI energy seen in figure 3. The BVISPL FFT metric is more affected by the higher frequency information in the noise signal, and so identifies a peak BVISPL further beneath the rotor system at an elevation of $\approx -70^\circ$. Contrary to this, the extracted BVISPL technique is dominated more by the peak to peak sound pressure levels, and so peak BVI noise is identified closer to an elevation of $\approx -45^\circ$, in figure 3a. As a consequence, the extraction technique results in identification of a more compact region of BVI dominated noise than the standard FFT metric.

The last BVI location identified occurs at $(200^\circ, -28^\circ)$. The BVI noise here is considerably weaker than at either of the two peak BVI locations, and both metrics agree on this. However, the BVISPL FFT metric shows a slightly stronger signal than the extracted BVISPL metric, due to the stronger presence of the tail rotor in this direction. The final lo-

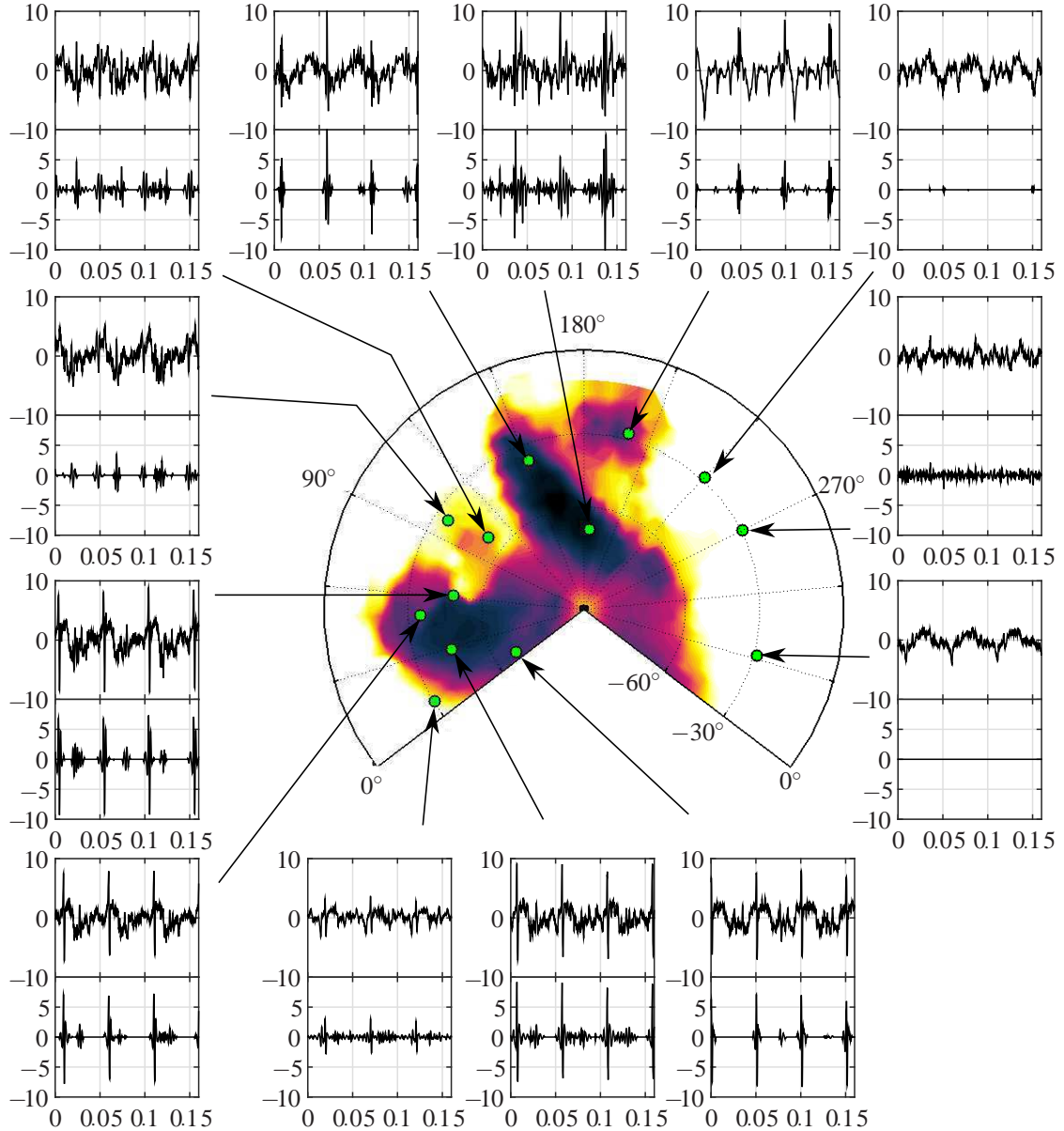


Fig. 4: BVI extraction hemisphere with representative original (top) and extracted (bottom) pressure signals.

cations of interest occur at $(240^\circ, -30^\circ)$, $(270^\circ, -30^\circ)$ and $(330^\circ, -30^\circ)$. At each of these locations, no BVI is seen in the raw pressure signal.

A weak, and erroneous, pressure signal is extracted by the BVI extraction technique at $(270^\circ, -30^\circ)$. This is a known deficiency of the technique, and occurs when energy in the main rotor harmonic blade passage frequency is small (Ref. 14). This allows the amplitude cutoff for the extraction technique to become very small, and so higher frequency data is extracted regardless of its origin. As the BVISPL is significantly beneath the peak BVI levels seen, this data can easily be discounted. To further prevent this data from being extracted, a minimum amplitude (E_{min}) could be identified for each vehicle and maneuver. This would result in equation (5) being modified as provided in equation (6).

One feature provided by the BVI extraction technique, is

the ability to identify BVI signals that originate from individual blades. However, as there is no once per revolution signal from the main rotor, there is no current way to link ‘Blade 1’ to a specific blade on the vehicle. Therefore, discussion of individual blade to blade differences in BVI noise is conducted for only a single descent run.

After extracting BVI signals from the raw pressure series, BVI signals can be identified by their peak positive pressure and synced with the blade passage frequency. All microphones can then be aligned by matching time of emission for each BVI event. Thus, each BVI event is assigned a corresponding blade number that is uniform across all microphones. Lambert projections of the BVI noise for each blade

can then be created. This process has been accomplished,

$$\tilde{p}(f_j, t_i) = \begin{cases} \tilde{p}(f_j, t_i) & \text{if } f_j > f_{cut} \text{ and} \\ & E(f_j, t_i) > E(f_{MR}, t_i) - A_{cut} \geq E_{min} \\ 0 & \text{otherwise} \end{cases} \quad (6)$$

resulting in the peak to peak BVI pressure signals provided for each blade passage in figure 5.

All values in figure 5 are in Pascals, and extracted from the same run as provided in figures 3 and 4. Thus, figure 5d, which comprises the average of all peak to peak BVI pressure amplitudes in Pascals, compares directly to the dB metric provided in figure 3a.

Lambert projections of peak to peak BVI pressure amplitudes and directivities identified for each blade are almost identical to that seen in figure 3a. A slight shift in directivity can be seen for the forward propagating BVI signal for blade 3, provided in figure 5c. However, all other features appear uniform between each blade. This implies that little blade to blade variation in BVI noise is present for this vehicle.

Test Condition Results

Having established the validity of the BVI extraction technique for use with the AS350B vehicle, we can now begin to investigate the differences between the four test conditions. The four test conditions include 6° descents at 80 KIAS and 80 KTAS for both take-off weights of 4400 ($C_w = 4.13 \cdot 10^{-3}$) and 3915 pounds ($C_w = 3.68 \cdot 10^{-3}$). The indicated airspeed required to fly 80 KTAS was calculated individually for each run as it is a function of density, which varies throughout the day with temperature. A typical 80 KTAS case is equivalent to 73 KIAS for this test location.

The BVI extraction technique is applied to at least 11 runs of each test condition. The number of runs included in the average for each condition are identified in table 2. An average

Table 2: Equivalent speeds as well as number of individual runs averaged for each test condition.

	KIAS	KTAS	4400	3915 [lb]
80 KIAS	80	87 (Typ)	11	13
80 KTAS	73 (Typ)	80	12	13

peak to peak BVI pressure signal, per BVI event, is then calculated for each condition and is provided in figure 6. Each test condition provides a unique directivity and strength of the active blade-vortex interaction noise signals.

The averaged, 4400 lb, 80 KIAS condition shown in figure 6a includes data from the individual run shown in figure 3a. While figure 6a is calculated using a different metric than used in figure 3a, similar BVI directivities are seen. Figure 6a shows a strong BVI signal propagating forward of the vehicle ($\approx 155^\circ, -45^\circ$), as well as a secondary interaction propagating behind and beneath the rotor ($\approx 45^\circ, -60^\circ$). This condition is identical to the instantaneous values shown previously

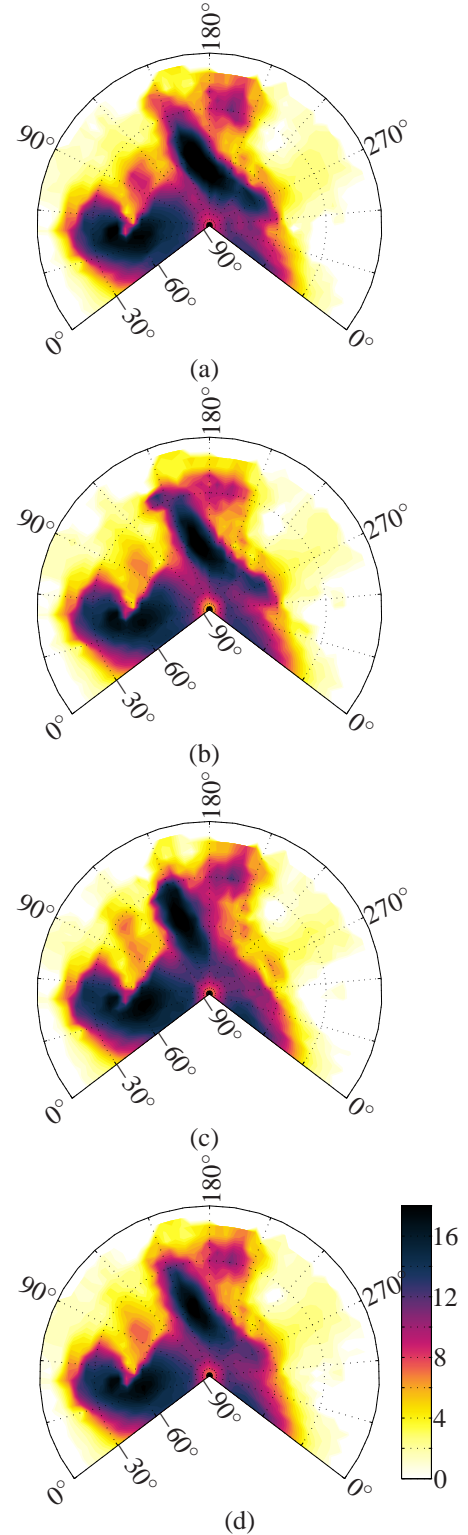
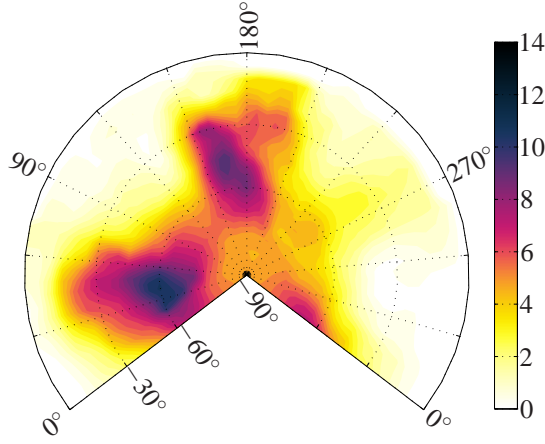


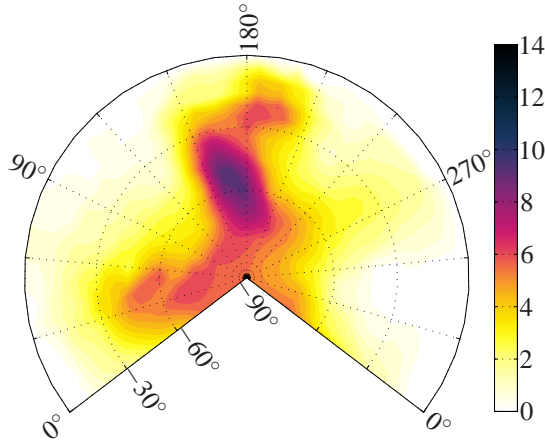
Fig. 5: Peak to peak BVI amplitudes, in Pascal, corresponding to blade (a) 1, (b) 2, and (c) 3 throughout an 80 knot IAS flight. (d) Average peak to peak BVI pressure amplitudes.

in figures 3 and 4. Contrary to this, the light 80 KIAS condition (figure 6b), shows a weaker forward propagating BVI signal, and a much weaker secondary interaction.

The less intense, forward propagating signal is expected for the light, 80 KIAS condition, as the vehicle weight is non-



(a)



(b)

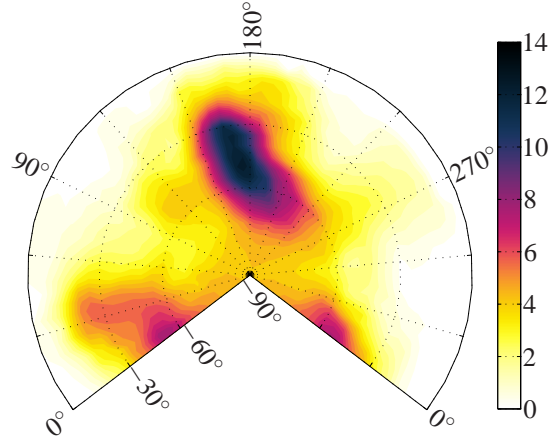
Fig. 6: Extracted BVI peak to peak pressure amplitudes [Pa] for (a) 4400 lb and (b) 3915 lb, 80 KIAS test condition.

inally 11% less than the heavier condition. However, the rearward propagating BVI signal is almost non-existent. Assuming that the aerodynamic state of the helicopter is identical to the previous condition, this change in BVI intensity is not adequately explained by changes in vehicle thrust alone. To first order, changes in vehicle thrust are related to BVI amplitude as

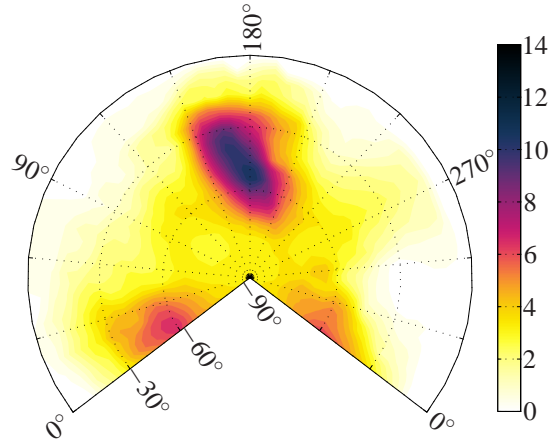
$$\Delta_{BVI} = 20 \log_{10} \left(\frac{W_1}{W_2} \right) \text{ [dB]}. \quad (7)$$

Here, Δ_{BVI} is the dB change in sound pressure level for thrust variations between two weights, identified as W_1 and W_2 , respectively (Ref. 14). Therefore, an 11% change in thrust would result in approximately 1 dB change in sound pressure level, corresponding with a 1 Pa change in peak to peak pressure levels. The maximum weight difference between heaviest and lightest run is 17%, when accounting for fuel burn, which would result in a difference of 1.3 dB, or peak to peak pressure difference of 1.17 Pa. Thus, weight variation affecting thrust levels does not adequately explain the 3 Pa peak to peak pressure level change seen on the forward propagating BVI signal, nor the 6 Pa change in peak to peak pressure level seen on the rearward propagating signal.

Tip-path-plane angle of attack could provide one possibility for the difference seen in the two weight conditions. Tip-



(a)



(b)

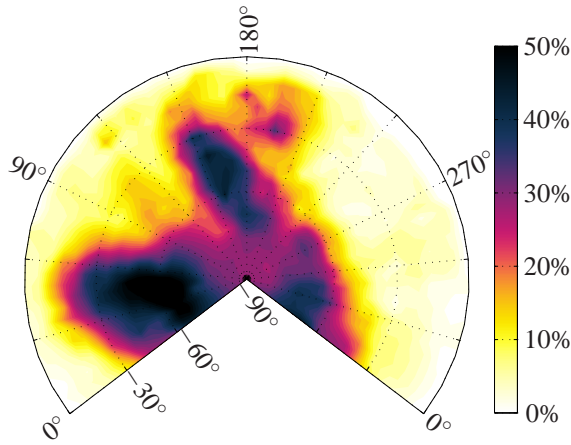
Fig. 7: Extracted BVI peak to peak pressure amplitudes [Pa] for (a) 4400 lb and (b) 3915 lb, 80 KTAS test condition.

path-plane angle (α) can be estimated to first order as,

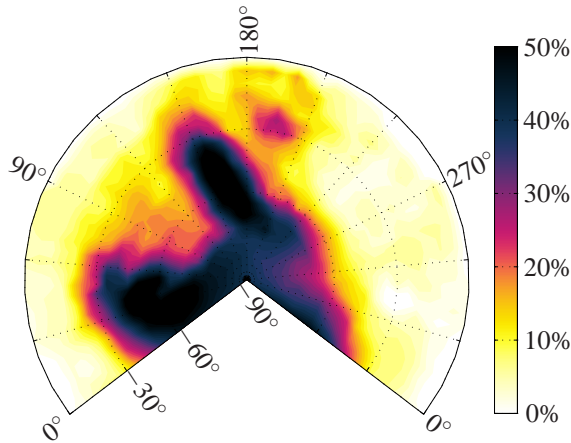
$$\alpha = -\frac{D}{W} - \gamma, \quad (8)$$

where γ, D, W are flightpath angle, drag, and weight, respectively. Drag is constant for a given true airspeed, and so similar flight profiles result in an inversely proportional relationship between tip-path-plane angle and vehicle weight. Therefore, the heavier condition would have a lower tip-path-plane angle due to requiring more thrust, resulting in a smaller miss distance and therefore higher BVI noise amplitudes. There are competing elements, however, as the higher thrust case would subsequently cause an increased inflow, and thereby increased miss distance. Further research is necessary to determine exactly why there are such drastic differences seen in figure 6. However, these results strongly suggest that future prediction techniques must account for payload, and possibly fuel burn rate, to adequately predict the acoustic footprint of a vehicle.

The last two conditions investigated are 80 KTAS descents, shown in figure 7. Figure 7 shows a forward propagating BVI signal at approximately $(160^\circ, -30^\circ)$, and a secondary signal that propagates directly behind the rotor at approximately $(0^\circ, -50^\circ)$. As expected, the heavier (4400 lb) condition presents each blade-vortex interaction noise as being stronger than in the lighter condition.



(a)



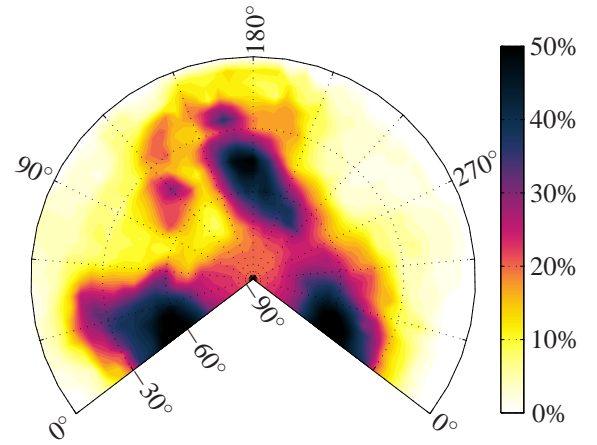
(b)

Fig. 8: Standard deviation of extracted BVI peak to peak pressure for for (a) 4400 lb and (b) 3915 lb, 80 KIAS test condition. Standard deviations are calculated from (a) 11 and (b) 13 individual runs, and are normalized by maximum peak to peak pressure (≈ 14 Pa).

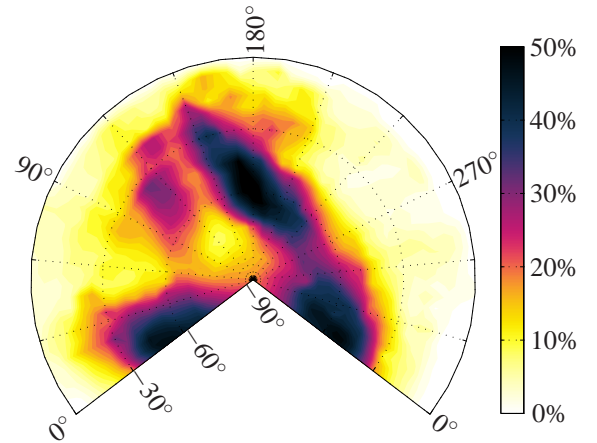
In opposition to the 80 KIAS condition, shown in figure 6, each interaction is still uniquely present between the two 80 KTAS conditions shown in figure 7. The 80 KIAS is flown at the same indicated airspeed, regardless of current weather conditions. Contrary to this, the KIAS equivalent of 80 KTAS is adjusted, prior to each run, based on the current temperature and pressure at flight altitude. This results in a closer match of the advancing tip-Mach number, and advance ratio, for the 80 KTAS condition. Therefore, the 80 KTAS condition provides a more consistent aerodynamic condition than what is provided by the 80 KIAS.

Figures 8 and 9 are normalized standard deviations of peak to peak pressure for each of the test conditions. Standard deviations are normalized by the maximum peak to peak value for each condition (≈ 14 Pa). As a whole, these figures suggest that the BVI noise signal fluctuates around 40-50% of the peak value wherever BVI is occurring.

The 80 KIAS descent conditions, shown in figure 8, display peak fluctuating BVI pressures along both the forward and rearward propagating BVI noise signals. Most importantly, however, it shows that the BVI signal on the early ad-



(a)



(b)

Fig. 9: Standard deviation of extracted BVI peak to peak pressure for for (a) 4400 lb and (b) 3915 lb, 80 KTAS test condition. Standard deviations are calculated from (a) 12 and (b) 13 individual runs, and are normalized by maximum peak to peak pressure (≈ 14 Pa).

vancing side of the 3915 lb condition has a standard deviation as large as those seen on the 4400 lb condition. This is contrary to what was seen for the peak to peak amplitudes shown in figure 6. This suggests that the lighter vehicle is operating near, but not consistently in, an aerodynamic condition where strong rearward propagating BVI occurs. This would result in rearward propagating BVI signal being absent during some flights, and strongly present in others; resulting in a lower average BVI peak to peak pressure signal but high standard deviation between runs.

The 80 KTAS descent condition (figure 9) displays almost identical BVI noise amplitude fluctuations between the two weight conditions. This was expected, as the peak to peak amplitudes, shown in figure 7, are also very similar. This further confirms that operating a vehicle based on true airspeed, and not the standard indicated airspeed, provides for more consistent acoustic results.

One key region should be noted in figure 9. The region of note is the 25-30% fluctuating pressure seen just slightly to the advancing side of the main, forward propagating BVI noise signal ($110^\circ, -45^\circ$). The raw and BVI extracted pres-

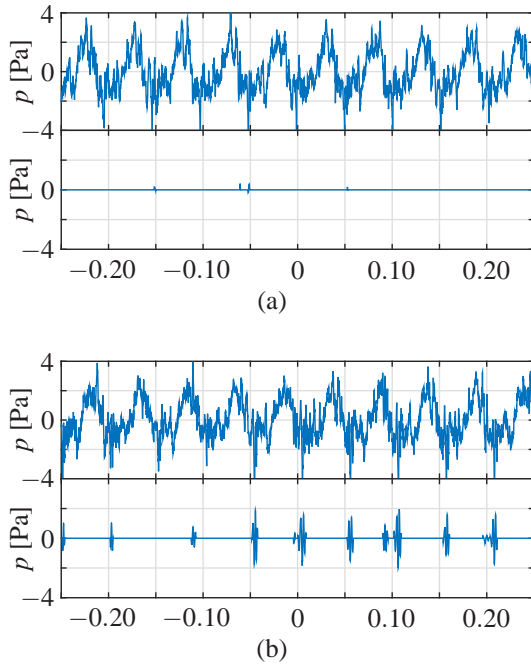


Fig. 10: Raw pressure signal as a function of time [s], centered on location $(110^\circ, -45^\circ)$ from two individual runs of the 3915 lb, 80 KTAS condition.

sure signals, shown in figure 10 for two separate runs, demonstrate that the BVI noise in this direction is intermittent. This signal is most likely caused by an intermittent, retreating side oblique BVI interaction. The BVI signal can be identified as a retreating side interaction due to it arriving after the peak positive pressure signal from blade passage, as well as the predominantly negative pressure pulses comprising the signal.

Conclusions

An initial investigation into BVI noise emitted by a full-scale AS350B vehicle during multiple descent conditions was conducted. Data from the AS350B was acquired during the Fall of 2014, in Sweetwater, NV at 7000 foot elevation. Four 6 degree descent conditions were focused on. Each descent condition was flown at least 11 times, and was flown at 80 knots indicated airspeed as well as 80 knots true airspeed. Each airspeed was flown for two take-off weights of 4400 and 3915 pounds.

A BVI extraction technique was employed on the experimentally acquired data to investigate the BVI noise signal in isolation. This extraction technique was compared to the standard BVISPL FFT method, and was shown to provide better BVI noise localization, as it is not as strongly corrupted by tail rotor and other higher frequency noise sources. The technique was also used to separate BVI noise resulting from each blade, where it was shown that this vehicle emitted little blade to blade differences in BVI noise. Further, it was shown that standard deviations in the peak to peak BVI pressures occur only in the directions where BVI occurs, and at values approximately 40-50% of the maximum peak to peak noise amplitude.

The most important result of this study, however, is that significant BVI noise amplitude changes can occur for the same flight condition flown at different vehicle weights. These changes are not adequately explained by changes in vehicle thrust alone, which should result in a linear increase in BVI noise. Instead, changes in vehicle weight must also affect vortex miss distance by way of changes to the tip-path-plane angle of attack, as well as induced inflow. This suggests that future acoustic prediction techniques need to incorporate payload, and possibly fuel burn information, in order to accurately predict noise footprints.

References

- ¹Schmitz, F. H., Boxwell, D. A., Lewy, S., and Dahan, C., "In-Flight Far-Field Measurement of Helicopter Impulsive Noise," *American Helicopter Society 32nd Annual Forum*, 1976.
- ²Martin, R. M. and Hardin, J. C., "Spectral Characteristics of Rotor Blade/Vortex Interaction Noise," *Journal of Aircraft*, Vol. 25, (1), 1988, pp. 62–68.
- ³Lowson, M. V., "Focusing on Helicopter BVI Noise," *Journal of Sound and Vibration*, Vol. 190, (3), 1996, pp. 477–494.
- ⁴Lim, J. W., Potsdam, M., Strawn, R., Sim, B. W.-C., and Nygaard, T., "Blade-Vortex Interaction Airloads Prediction Using Multidisciplinary Coupling," *HPCMP Users Group Conference*, 2006.
- ⁵Schmitz, F. H. and Yu, Y. H., "Helicopter impulsive noise: Theoretical and experimental status," *Journal of Sound and Vibration*, Vol. 109, (3), 1986, pp. 361–422.
- ⁶Widnall, S., "Helicopter Noise due to Blade-Vortex Interaction," *Journal of the Acoustical Society of America*, Vol. 50, (1), 1971, pp. 354–365.
- ⁷Sim, B. W.-C. and Lim, J. W., "Blade-Vortex Interaction (BVI) Noise & Airload Prediction Using Loose Aerodynamic/Structural Coupling," *American Helicopter Society 62nd Annual Forum*, 2006.
- ⁸Davis, W., Pezeshki, C., and Mosher, M., "Extracting and Characterizing Blade-Vortex Interaction Noise with Wavelets," *Journal of the American Helicopter Society*, Vol. 42, (3), 1997, pp. 264–271.
- ⁹Sickenberger, R., Gopalan, G., and Schmitz, F. H., "Helicopter Near-Horizon Harmonic Noise Radiation due to Cyclic Pitch Transient Control," *American Helicopter Society 67th Annual Forum*, 2011.
- ¹⁰Stephenson, J. H. and Tinney, C. E., "Time frequency analysis of sound from a maneuvering rotorcraft," *American Helicopter Society 70th Annual Forum*, 2014.
- ¹¹Stephenson, J. H., Tinney, C. E., Greenwood, E., and Watts, M. E., "Extracting Blade Vortex Interactions using Continuous Wavelet Transforms," *Journal of Sound and Vibration*, Vol. 333, (21), 2014, pp. 5324–5339.

¹²Torrence, C. and Compo, G. P., “A Practical Guide to Wavelet Analysis,” *Bulletin of the American Meteorological Society*, Vol. 79, (1), 1998, pp. 61–78.

¹³Farge, M., “Wavelet Transforms and their Applications to Turbulence,” *Annual Review of Fluid Mechanics*, Vol. 24, 1998, pp. 395–457.

¹⁴Stephenson, J. H., *Extraction of Blade Vortex Interactions from Helicopter Transient Maneuvering Noise*, Ph.D. thesis, University of Texas at Austin, 2014.

¹⁵Greenwood, E. and Schmitz, F. H., “Separation of Main and Tail Rotor Noise Ground-Based Acoustic Measurements,” *Journal of Aircraft*, Vol. 51, (2), 2014, pp. 464–472.